applied sciences

MDPI

Article

The Interphase Influences on the Particle-Reinforced Composites with Periodic Particle Configuration

Junjie Ye [1,2,*], Chenchen Chu [1], Zhi Zhai [3], Yongkun Wang [1], Baoquan Shi [2] and Yuanying Qiu [1]

1 Key Laboratory of Ministry of Education for Electronic Equipment Structure Design, Xidian University, Xi'an 710071, China; ccc@stu.xidian.edu.cn (C.C.); ykwang@xidian.edu.cn (Y.W.); yyqiu@mail.xidian.edu.cn (Y.Q.)

2 Research Center for Applied Mechanics, Xidian University, Xi'an 710071, China; xjtushbq@163.com

3 State Key Laboratory for Manufacturing Systems Engineering, Xi'an Jiaotong University, Xi'an 710049, China; zhaizhi_emler@sina.com

* Correspondence: ronkey6000@sina.com; Tel.: +86-29-8820-4639

Academic Editor: Patrick A. Fairclough

Received: 29 November 2016; Accepted: 12 January 2017; Published: 23 January 2017

Abstract: This work improved upon an effective micromechanical method to analyze the mechanical properties of three-dimensional particle-reinforced composites (PRC) with consideration of the interfacial debonding. By incorporating the interfacial debonding model, Mises yield criterion, and failure theory, the effects of particle shape, particle volume fraction, and loading condition on the mechanical properties are studied. A comparison of simulation results obtained from the established method and published experimental data is presented. Good consistency can be found in this study. On this basis, the interfacial cohesive strength and particle shape effects on the biaxial failure strength of particle-reinforced composites with interfacial debonding were also studied. The results revealed that both interfacial strength and particle shape have significant effects on biaxial tensile failure strength. However, the different interfacial strength influence on failure envelope can hardly be discerned in biaxial compressive loading.

Keywords: 3-dimensional reinforced composites; interphase; microstructures

1. Introduction

With the rapid development of modern industrial technology, particle-reinforced metal matrix composites, which combine the ductility and toughness of metal phase with the high strength of the reinforced particles, have been widely used due to their high specific strength and high specific rigidity [1–4]. As is well known, the mechanical behaviors of composites with complex microstructures are closely dependent on many factors, such as inclusion volume fraction, inclusion shapes, etc. The higher stiffness behaviors of composites can be achieved by increasing the particle volume fraction (PVF) and improving the manufacturing technology [5,6]. However, increasing the volume fraction often decreases the ductility of composites. Therefore, it is important for designers to consider some certain factors including the PVF, interphase between particles and matrix, and particle size when determining the mechanical properties.

For estimating the particle size [7–10] and particle shape [11,12] effect on the mechanical properties, the representative volume element (RVE) is always used to establish the mechanical model [13–16]. At present, a number of modeling techniques have been proposed. The strain-gradient plasticity models have been used by Gao and Huang [17,18] to study particle size effect and interface fracture in aluminum alloy composites. Abedini and Chen [19] modified the tangent-based homogenization method with incorporation of dislocation strengthening. It was revealed that the nonlinear behaviors of composites in uniaxial tension are based upon particle size and PVF. McWilliams et al. [20] presented

an enhanced continuum model to explore the effects of particle size and volume fraction on the variability of the inelastic deformation response of particle-reinforced metal matrix composites. It was revealed that the variance of the composite response increases as particle size decreases and as the volume fraction of reinforcing particles increases. Zhang et al. [21] employed the finite element method to calculate the average coefficient of thermal expansion, Young's modulus, and Poisson's ratio. Moumen et al. [22] combined the finite element method with statistical methods to study the elastic properties of composites with natural particle fillers.

In order to investigate the effect of the interphase between the particles and matrix, a number of numerical techniques have been improved in the literature [23–27]. By incorporating the dislocation punched zone model, cohesive zone model, and the Taylor-based nonlocal theory, an enhanced finite element method (FEM) was proposed by Shao et al. [28] to investigate the effect of interfacial debonding in the particle-reinforced metal matrix composites. Yuan et al. [29] combined the cohesive element technique with the finite element method to study the effect of the interface thickness and strength. It was shown that the particle shape and interface geometry strongly influenced the distribution of the stress states. Based on the coupled stress and energy criterion of the finite fracture mechanics (FFM), García [30] proposed a theoretical model to study the influence of the interface properties. From the investigations mentioned above, the researchers have always paid attention to the analysis of interfacial debonding effects on nonlinear stress-strain behaviors. Aghdam and Shahbaz [31] employed the micromechanical FEM to predict the interphase damage and residual stresses effect on the mechanical behaviors of particle-reinforced composites (PRC). Majer et al. [32] employed the commercial finite-element code ANSYS to establish a three-phase model consisting of a matrix, particles, and an interphase, in order to investigate the fracture behaviors of particulate polymer composites. However, few previous studies have systematically studied the interfacial bonding properties effect on the biaxial failure strength of the PRC.

The present study aimed to conduct an in-depth study of the relations between macroscopic mechanical properties and intrinsic microstructure parameters (particle shape, particle volume fraction), as well as extrinsic parameters (strain rate) of the PRC with consideration of interfacial debonding. To this end, the periodic unit cell was employed. The outline is as follows. Based on the microstructure of the RVE, the constitutive relations of the PRC with interfacial debonding are established in Section 2. In Section 3, the nonlinear stress-strain behaviors of the PRC with interfacial debonding are studied. The theoretical results show a good agreement with the experimental data. Furthermore, the particle shape and interfacial cohesive strength effects on the biaxial failure envelopes of the PRC with interfacial debonding are investigated in Section 4. The conclusions are shown in Section 5.

2. The Theoretical Method

2.1. Microstructure of the RVE

The particle-reinforced composites (PRC) are prepared through a specific process by blending the particles into the matrix materials. Due to their different material properties, the interphase between particles and matrix material shows complex stress states in loading. The interfacial failure becomes one of the most important factors, which leads to the structural fracture. Here, the idealized uniform size particles with interphase are considered to be periodically distributed in the matrix. The 3-dimensional representative volume element (RVE) is also considered, as shown in Figure 1. The particle and interface between the particle and matrix are denoted by pale yellow and gray, respectively. The RVE consist of $N_\alpha \times N_\beta \times N_\gamma$ sub-cells, and the number of sub-cells are labeled as α, β, and γ along with the x-, y-, and z-direction, as shown in Figure 1a. Furthermore, the interfacial phase is considered to be relative thin, and the thickness can be ignored. The dimensions of the RVE are defined as d, h, and l along with the x-, y-, and z-direction, as shown in Figure 1b. The dimensions of the particle are defined as a, b, and c along with the x-, y-, and z-direction. Meanwhile, the geometric centers of the particle and the RVE coincide with each other.

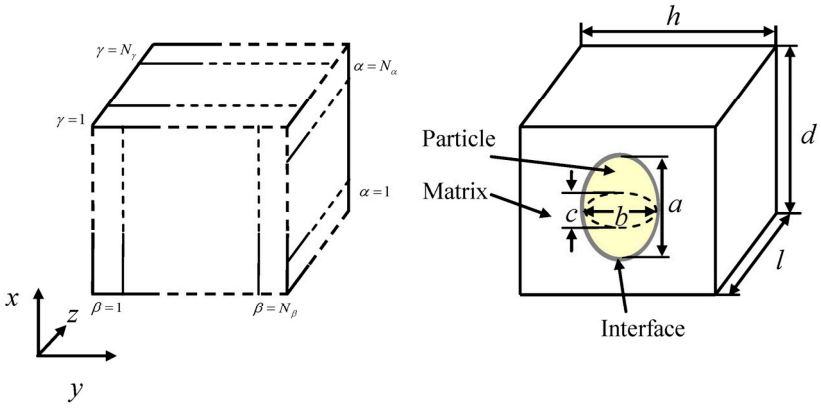

(**a**) (**b**)

Figure 1. The 3-demensional representative volume element (RVE) (**a**) Discretization of the RVE; (**b**) An inclusion in the RVE.

2.2. Constitutive Equations of the PRC with Interfacial Debonding

The RVE consist of a certain number of cubic sub-cells, denoted by the parameters α, β, and γ, as shown in Figure 1a. Each sub-cell contains an elastic or inelastic material. Therefore, the different microstructures can be acquired by filling appropriate particle or matrix materials in the RVE. The constitutive relations between the sub-cell strain $\boldsymbol{\varepsilon}^{(\alpha\beta\gamma)}$ and sub-cell stress $\boldsymbol{\sigma}^{(\alpha\beta\gamma)}$ can be written as follows:

$$\boldsymbol{\varepsilon}^{(\alpha\beta\gamma)} = \mathbf{S}^{(\alpha\beta\gamma)}\boldsymbol{\sigma}^{(\alpha\beta\gamma)} + \boldsymbol{\varepsilon}^{I(\alpha\beta\gamma)} + \boldsymbol{\alpha}^{(\alpha\beta\gamma)}\Delta T \tag{1}$$

where $\mathbf{S}^{(\alpha\beta\gamma)}$ and $\boldsymbol{\varepsilon}^{I(\alpha\beta\gamma)}$ indicate the sub-cell compliance matrix and inelastic strain matrix, respectively. The parameters $\boldsymbol{\alpha}^{(\alpha\beta\gamma)}$ and ΔT are the sub-cell thermal expansion coefficient and temperature variation, respectively.

According to the generalized method of cells (GMC) micromechanical model, which is proposed by Aboudi [33,34], the relations between the average strain rates and sub-cell strain rates for the PRC can be written as:

$$\mathbf{A}_G\dot{\bar{\boldsymbol{\varepsilon}}}_s = \mathbf{J}\dot{\bar{\boldsymbol{\varepsilon}}} \tag{2}$$

where $\dot{\bar{\boldsymbol{\varepsilon}}}$ indicates the average strain rate vector $(\dot{\bar{\varepsilon}}_{11}, \dot{\bar{\varepsilon}}_{22}, \dot{\bar{\varepsilon}}_{33}, 2\dot{\bar{\varepsilon}}_{23}, 2\dot{\bar{\varepsilon}}_{13}, 2\dot{\bar{\varepsilon}}_{12})$. The matrix $\mathbf{A}_G$ and the vector $\boldsymbol{J}$ contain the sub-cell dimensions and the RVE dimensions, respectively. The vector $\dot{\bar{\boldsymbol{\varepsilon}}}_s$ indicates the sub-cell strain rate vector $(\dot{\bar{\varepsilon}}^{111}, \ldots, \dot{\bar{\varepsilon}}^{N_\alpha N_\beta N_\gamma})$.

For describing the interfacial debonding effects on the mechanical properties of the PRC, the evolving compliant interface model, one of the interfacial debonding models, is introduced. The interfacial displacement $\dot{u}_{ij}^I$ between the particles and matrix can be written as follows [35]:

$$\dot{u}_{ij}^I = \dot{R}_{ij}\sigma_{ij}^I + R_{ij}\dot{\sigma}_{ij}^I (i,j = 1,2,3) \tag{3}$$

where R_{ij} and σ_{ij}^I indicate the interfacial debonding parameters and interfacial stress components, respectively. The dotted terms indicate the derivative of a variation with respect to time.

The interfacial stress components along with *x*-, *y*-, and *z*-direction between the particle and matrix are continuously required, while the displacement components are discontinuous. The micromechanical model in Equation (2) should be modified as follows:

$$\sum_{\alpha=1}^{N_\alpha} (d_\alpha \dot{\bar{\varepsilon}}_{11}^{\alpha\beta\gamma} + \dot{u}_{11}^{\alpha\beta\gamma}) = d\dot{\bar{\varepsilon}}_{11} \tag{4}$$

$$\sum_{\beta=1}^{N_\beta} (h_\beta \dot{\bar{\varepsilon}}_{22}^{\alpha\beta\gamma} + \dot{u}_{22}^{\alpha\beta\gamma}) = h\dot{\bar{\varepsilon}}_{22} \tag{5}$$

$$\sum_{\gamma=1}^{N_\gamma} (l_\gamma \dot{\bar{\varepsilon}}_{33}^{\alpha\beta\gamma} + \dot{u}_{33}^{\alpha\beta\gamma}) = l\dot{\bar{\varepsilon}}_{33} \tag{6}$$

$$\sum_{\alpha=1}^{N_\alpha}\sum_{\beta=1}^{N_\beta} (d_\alpha h_\beta \dot{\bar{\varepsilon}}_{12}^{\alpha\beta\gamma} + h_\beta \dot{u}_{12}^{\alpha\beta\gamma} + d_\alpha \dot{u}_{21}^{\alpha\beta\gamma}) = dh\dot{\bar{\varepsilon}}_{12} \tag{7}$$

$$\sum_{\beta=1}^{N_\beta}\sum_{\gamma=1}^{N_\gamma} (h_\beta l_\gamma \dot{\bar{\varepsilon}}_{23}^{\alpha\beta\gamma} + l_\gamma \dot{u}_{23}^{\alpha\beta\gamma} + h_\beta \dot{u}_{32}^{\alpha\beta\gamma}) = hl\dot{\bar{\varepsilon}}_{23} \tag{8}$$

$$\sum_{\alpha=1}^{N_\alpha}\sum_{\gamma=1}^{N_\gamma} (d_\alpha l_\gamma \dot{\bar{\varepsilon}}_{23}^{\alpha\beta\gamma} + l_\gamma \dot{u}_{13}^{\alpha\beta\gamma} + d_\alpha \dot{u}_{31}^{\alpha\beta\gamma}) = dl\dot{\bar{\varepsilon}}_{13} \tag{9}$$

where the parameters d_α, h_β, and l_γ indicate the sub-cell dimensions along with the x-, y-, and z-direction.

Taking use of the numerical integral method with respective to Equation (4)–(9), as well as combining the interfacial stress continuous condition with the constitutive relations in Equation (1), the sub-cell stresses can be written as the matrix forms, that is:

$$\mathbf{GT} = \boldsymbol{\varepsilon}^{E(\alpha\beta\gamma)} - \boldsymbol{\varepsilon}^{I(\alpha\beta\gamma)} - \boldsymbol{\alpha}^{T(\alpha\beta\gamma)}\Delta T \tag{10}$$

where $\boldsymbol{\varepsilon}^{E(\alpha\beta\gamma)}$ indicates the average elastic strain vector $(d\varepsilon_{11}, h\varepsilon_{22}, l\varepsilon_{33}, 2hl\varepsilon_{23}, 2dl\varepsilon_{13}, 2dh\varepsilon_{12})^{\mathrm{T}}$. The variations $\boldsymbol{\varepsilon}^{E(\alpha\beta\gamma)}$ denote the inelastic strain components of the sub-cell $(\sum_\beta d_\alpha \varepsilon_{11}^{I(\alpha\beta\gamma)} \sum_\beta h_\beta \varepsilon_{22}^{I(\alpha\beta\gamma)} \sum_\beta l_\gamma \varepsilon_{33}^{I(\alpha\beta\gamma)} 2\sum_\beta\sum_\gamma h_\beta l_\gamma \varepsilon_{23}^{I(\alpha\beta\gamma)} 2\sum_\alpha\sum_\gamma d_\alpha l_\gamma \varepsilon_{13}^{I(\alpha\beta\gamma)} 2\sum_\alpha\sum_\gamma d_\alpha h_\beta \varepsilon_{12}^{I(\alpha\beta\gamma)})^{\mathrm{T}}$. $\boldsymbol{T}$ is the stress component $(T_{11}^{\beta\gamma}, T_{22}^{\alpha\gamma}, T_{33}^{\alpha\beta}, T_{23}^{\alpha}, T_{13}^{\beta}, T_{12}^{\gamma})^{T}$. It should be noted that the component $T_{11}^{\beta\gamma}$ indicates the sub-cell stress $\sigma_{11}^{\alpha\beta\gamma}$. From Figure 1, it can be seen that $\sigma_{11}^{\alpha\beta\gamma}$ is a constant along the x-direction. Therefore, the superscript α in the sub-cell stress component $\sigma_{11}^{\alpha\beta\gamma}$ along with the x-direction is omitted and the component is written as $T_{11}^{\beta\gamma}$. Similar presentations are shown in the sub-cell stress components $T_{22}^{\alpha\gamma}$ and $T_{33}^{\alpha\beta}$. The variation T_{23}^{α} indicates the sub-cell shear stress components $\sigma_{23}^{\alpha\beta\gamma}$ along the x-direction. For each sub-cell, the subscript indicates the sub-cell shear stress, and the stress component has a constant value along the x-direction. Therefore, the superscripts β and γ in the sub-cell stress component are omitted. Similar presentations are shown in the sub-cell shear stress components T_{13}^{β} and T_{12}^{γ}. The variations $\boldsymbol{\alpha}^{\mathrm{T}(\alpha\beta\gamma)}$ indicate the sub-cell thermal expansion coefficient and they can be written as $(\sum_\beta d_\alpha \alpha_{11}^{\alpha\beta\gamma} \sum_\beta h_\beta \alpha_{22}^{\alpha\beta\gamma} \sum_\beta l_\gamma \alpha_{33}^{\alpha\beta\gamma} 2\sum_\beta\sum_\gamma h_\beta l_\gamma \alpha_{23}^{\alpha\beta\gamma} 2\sum_\alpha\sum_\gamma d_\alpha l_\gamma \alpha_{13}^{\alpha\beta\gamma} 2\sum_\alpha\sum_\gamma d_\alpha h_\beta \alpha_{12}^{\alpha\beta\gamma})^{\mathrm{T}}$. The specific forms of the matrix G in the expression mentioned above can be written as follows:

$$G = \begin{bmatrix}
\sum_\alpha d_\alpha S_{11}^{\alpha\beta\gamma} R_{11}^{\beta\gamma} & \sum_\alpha d_\alpha S_{12}^{\alpha\beta\gamma} & \sum_\alpha d_\alpha S_{13}^{\alpha\beta\gamma} & \sum_\alpha d_\alpha S_{14}^{\alpha\beta\gamma} & \sum_\alpha d_\alpha S_{15}^{\alpha\beta\gamma} & \sum_\alpha d_\alpha S_{16}^{\alpha\beta\gamma} \\
\sum_\beta h_\beta S_{12}^{\alpha\beta\gamma} & \sum_\beta h_\beta S_{22}^{\alpha\beta\gamma} R_{22}^{\alpha\beta\gamma} & \sum_\beta h_\beta S_{23}^{\alpha\beta\gamma} & \sum_\beta h_\beta S_{24}^{\alpha\beta\gamma} & \sum_\beta h_\beta S_{25}^{\alpha\beta\gamma} & \sum_\beta h_\beta S_{26}^{\alpha\beta\gamma} \\
\sum_\gamma l_\gamma S_{13}^{\alpha\beta\gamma} & \sum_\gamma l_\gamma S_{23}^{\alpha\beta\gamma} & \sum_\gamma l_\gamma S_{33}^{\alpha\beta\gamma} R_{33}^{\alpha\beta\gamma} & \sum_\gamma l_\gamma S_{34}^{\alpha\beta\gamma} & \sum_\gamma l_\gamma S_{35}^{\alpha\beta\gamma} & \sum_\gamma l_\gamma S_{36}^{\alpha\beta\gamma} \\
\sum_\beta\sum_\gamma h_\beta l_\gamma S_{14}^{\alpha\beta\gamma} & \sum_\beta\sum_\gamma h_\beta l_\gamma S_{24}^{\alpha\beta\gamma} & \sum_\beta\sum_\gamma h_\beta l_\gamma S_{34}^{\alpha\beta\gamma} & \sum_\beta\sum_\gamma (h_\beta l_\gamma S_{44}^{\alpha\beta\gamma} + l_\gamma R_{23}^{\alpha\beta\gamma} + \sum_\beta h_\beta R_{32}^{\alpha\beta\gamma}) & \sum_\beta\sum_\gamma h_\beta l_\gamma S_{45}^{\alpha\beta\gamma} & \sum_\beta\sum_\gamma h_\beta l_\gamma S_{46}^{\alpha\beta\gamma} \\
\sum_\alpha\sum_\gamma d_\alpha l_\gamma S_{15}^{\alpha\beta\gamma} & \sum_\alpha\sum_\gamma d_\alpha l_\gamma S_{25}^{\alpha\beta\gamma} & \sum_\alpha\sum_\gamma d_\alpha l_\gamma S_{35}^{\alpha\beta\gamma} & \sum_\alpha\sum_\gamma d_\alpha l_\gamma S_{45}^{\alpha\beta\gamma} & \sum_\alpha\sum_\gamma (d_\alpha l_\gamma S_{55}^{\alpha\beta\gamma} + l_\gamma R_{13}^{\alpha\beta\gamma} + d_\alpha R_{31}^{\alpha\beta\gamma}) & \sum_\beta\sum_\gamma h_\beta l_\gamma S_{56}^{\alpha\beta\gamma} \\
\sum_\alpha\sum_\beta d_\alpha h_\beta S_{16}^{\alpha\beta\gamma} & \sum_\alpha\sum_\beta d_\alpha h_\beta S_{26}^{\alpha\beta\gamma} & \sum_\alpha\sum_\beta d_\alpha h_\beta S_{36}^{\alpha\beta\gamma} & \sum_\alpha\sum_\beta d_\alpha h_\beta S_{46}^{\alpha\beta\gamma} & \sum_\alpha\sum_\beta d_\alpha h_\beta S_{56}^{\alpha\beta\gamma} & \sum_\alpha\sum_\beta (d_\alpha h_\beta S_{66}^{\alpha\beta\gamma} + h_\beta R_{12}^{\alpha\beta\gamma} + d_\alpha R_{21}^{\alpha\beta\gamma})
\end{bmatrix}$$

By multiplying $\boldsymbol{G}^{-1}$ in Equation (10), the sub-cell stresses for the PRC with interfacial debonding can be obtained. For acquiring the macroscopic constitutive equation, the macroscopic stress components $\overline{\sigma}_{ij}$ based on homogenization theory can be written as follows:

$$\overline{\sigma}_{ij} = \frac{1}{dhl}\sum_{\alpha=1}^{N_\alpha}\sum_{\beta=1}^{N_\beta}\sum_{\gamma=1}^{N_\gamma} d_\alpha h_\beta l_\gamma \overline{\sigma}_{ij}^{\alpha\beta\gamma}(i,\ j=1,\ 2,\ 3\ ) \tag{11}$$

3. Nonlinear Mechanical Properties for the PRC with Interfacial Debonding

Composites show evident macroscopic and microscopic properties. In other words, their macroscopic mechanical responses are closely dependent on intrinsic microstructure parameters (particle shape, particle volume fraction), as well as extrinsic parameter (strain rate). SiC particle-reinforced A356 aluminum composites, which were quenched from manufacture temperature to room temperature, are studied in this present work. It is no doubt that the microstructure distribution of the SiC particles are closely dependent on the fabrication processing. In order to acquire the SiC/Al composites with the desired properties, it is important to choose the sizes of Al metal and SiC powders in order to avoid having leftover agglomerates after blending. Here, the spherical SiC particles with equivalent diameter 16 μm and PVF 15% are used to investigate the mechanical behaviors of SiC/Al composites according to the Lloyd [36]. The material properties of SiC particle and Al matrix materials are as follows [29,36,37]: the particle elastic modulus E_p = 427 Gpa. v_p = 0.17 is the Poisson's ratio and $\alpha_\mathrm{p} = 4.3 \times 10^{-6}/^\circ\mathrm{C}$ indicates the thermal expansion coefficient. For matrix materials, E_m = 76 Gpa is the Young's modulus. v_m = 0.33 is the Poisson's ratio. $\alpha_\mathrm{m} = 23.6 \times 10^{-6}/^\circ\mathrm{C}$ indicates the thermal expansion coefficient. The subscript p and m indicate the particle and matrix, respectively. Here, the SiC particles are assumed to have linear elasticity, and the Al matrix is assumed to have elasto-plasticity. In order to quantitatively describe the interfacial debonding effects on macroscopic mechanical responses, the interfacial cohesive strength between particles and matrix is assumed to be 430 MPa. The nonlinear stress-strain properties are described by using von Mises yield criterion and the yield strength of the matrix is 205 MPa. In addition, due to the mismatch of thermal expansion between particles and matrix, the thermal residual stresses, which are considered in all cases, will be produced in composites. At the manufacturing temperature of 780 °C, a zero strain condition for both the particle and the matrix is assumed.

3.1. Model Validation

In order to verify the present micromechanical method, the experimental results by Lyold [36] for the elastic constant and uniaxial tensile stress-strain behaviors are used. By using the micromechanical method for the spherical PRC (the ratio of *a*:*b*:*c* = 1:1:1 is as shown in Figure 1b), the elastic modulus is 94.4 GPa, which agrees well with the experimental results. Figure 2 shows the stress-strain behaviors of the spherical PRC. For comparing the interface properties effect on the macroscopic mechanical responses, composites with and without interfacial debonding are both considered. It can be found that the stress-strain responses in the linear elastic stage are unrelated with interfacial cohesion. As the loading strain increases, the theoretical results show higher stiffness behaviors than the experimental data for composites without consideration of interfacial debonding. The interfacial debonding influences on mechanical properties show a distinct difference when the true strain increases to 2.3%. Once the strain is greater than 2.3%, the interfacial debonding tends to decrease the stiffness behaviors sharply. In detail, compared with SiC/Al composites with interfacial debonding, the stress of composites with perfect interfaces provides a 27.9% increase when the true strain increases to 5%. Furthermore, compared with the experimental data [36], the theoretical relative error is less than 5% when the interfacial debonding is considered. Therefore, it should be denoted that the effective numerical method can be acquired only when the interfacial debonding is considered.

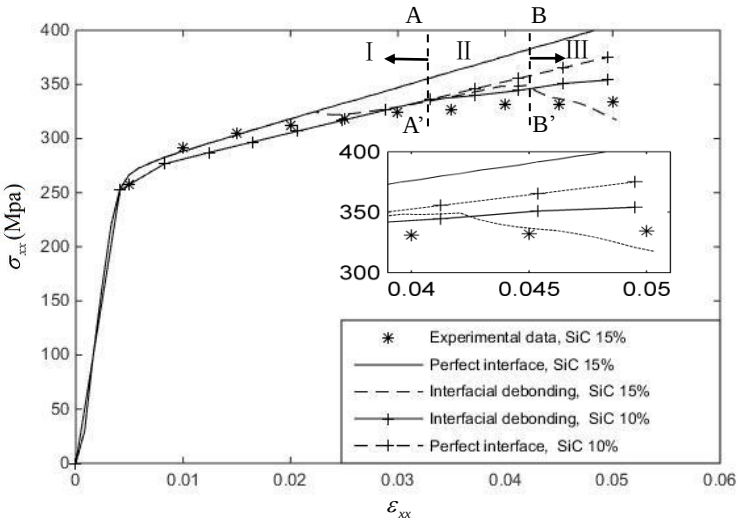

Figure 2. Stress-strain responses of composites with different particle volume fractions.

3.2. Intrinsic Microstructure Parameters

3.2.1. PVF Influences on the Mechanical Properties of the PRC

For investigating the PVF influences on uniaxial tensile properties, the mechanical behaviors of composites with 10% SiC particles were also considered and the results are plotted in Figure 2. The SiC/Al composites with and without the interfacial debonding are both considered in the example. It can be concluded that the mechanical properties of the PRC are closely related to the contact area and interfacial properties. Similar to 15% SiC composites, an obvious difference can be seen when the true strain increases to 3.7%. The stiffness properties tend to decrease when the interfacial debonding is considered. In addition, it is interesting to mention that the PVF effects on stiffness behaviors of the PRC with and without interfacial debonding show different variations. In detail, composites with higher PVF will yield more stiffening behaviors only if the interfacial debonding is ignored. Due to the particles restrained on the matrix, the higher stress can be transmitted to the reinforced particles through the matrix, and the stiffness behaviors can be obviously strengthened. However, a completely different phenomenon can be found when the interfacial debonding is considered. The PVF effects on the stiffness properties show evident regional characteristic. In detail, two sublines A-A′ and B-B′ are defined as shown in Figure 2. The sublines divided the strain region into three regions. On the left side of the subline A-A′ is defined as region I. On the right side of the subline B-B′ is defined as region III. The region between subline A-A′ and subline B-B′ is defined as region II. From Figure 2, it can be concluded that the constitutive behaviors become stiffer with the increasing volume fraction in region I. In contrast, an opposite conclusion can be reached in region III. That is, the increasing PVF tends to soften the stiffness behaviors for the particle-reinforced composites. This is due to the variation of interphase between particles and matrix. In other words, a higher PVF leads to an increase in contact region between the particles and matrix. Once interfacial debonding starts, less stress can be transmitted to SiC particles. Therefore, the Al matrix will support more loading which leads to the decrease of the stiffness properties.

3.2.2. Particle Shape Influences on the Mechanical Properties of the PRC

In order to investigate particle shape influences on mechanical properties of the PRC, the ellipsoid particle is introduced. The volume fraction of SiC particles is equal to 15%. For the ellipsoid particles, two different semi-major axis ratios denoted by a/b are 1.5 and 1.2, respectively. While the semi-minor ratios denoted by c/b are equal to 1.0. Here, the interfacial debonding influences on mechanical responses along with semi-major axis are investigated. Figure 3 shows that the mechanical properties

of the PRC are also dependent on interfacial properties when the particle shapes are considered. For comparison, the numerical results of the spherical PRC (the ratio of *a*:*b*:*c* = 1:1:1) as shown in Figure 2 are also plotted in Figure 3. It is difficult for researchers to discern the difference in the linear elastic stage. However, with the strain increase to the inelastic region, different effects of semi-major axis ratios on plastic deformation can be easily discerned. In detail, the higher semi-major axis ratios tend to stiffen the constitutive equation of composites without interfacial debonding. It is indicated that the higher semi-major axis ratio can improve the ability to resist the plastic deformation. In contrast, an opposite conclusion can be acquired for the PRC with interfacial debonding. This means that the stiffness of the PRC with semi-major axis ratio 1.5 is lower than the semi-major axis ratio 1.2 when the true strain is greater than 3.2%. This is due to the increase of the semi-major axis ratio, similar to the continuous fiber-reinforced composites [38,39]. Once the interfacial debonding occurs between particles and the matrix, less matrix region will undertake the overall stress. Compared with the PRC with the semi-major axis ratios of 1.5 and 1.2, the spherical PRC provides nearly a 7.9% and 6.7% increase when the true strain is equal to 0.04. It can be seen that the interfacial cohesive properties play an important role in studying mechanical behaviors when the interfacial stress reaches the cohesive strength.

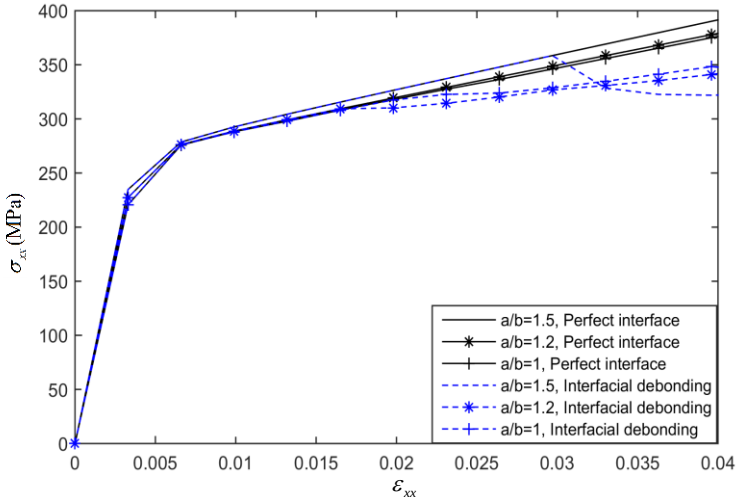

Figure 3. Stress-strain responses of composites with different particle shapes.

This is due to the stress concentration between particles and matrix. The lower strain rate provides enough time to relax stress concentration, which leads to the higher inelastic strain.

3.3. Extrinsic Parameter

Figure 4 shows the stress-strain curves of the PRC with different loading strain rates. The volume fraction of the SiC particles is 15%. The interfacial debonding and thermal residual stress are both considered in the cases. The reinforced phase is also assumed to involve spherical particles. Three different strain rates, namely 0.0005/s, 0.001/s, and 0.01/s, are considered. For continuous fiber-reinforced composites with perfect interfacial bonding [40], the strain rate affects the nonlinear responses, and it can be discerned but to a limit extent only in the nonlinear stage. Meanwhile, the higher strain rate tends to stiffen the constitutive behaviors. Similarly, the PRC shows obvious rate-dependency of the deformation. It is difficult to discern the effect of the different strain rates on the mechanical properties of the PRC with interfacial debonding in the linear elastic region. While the strain rate effects on the stress-strain behaviors can be easily discerned when the longitudinal strain ε_{xx} increases to 2.4% (the point C), as shown in the figure, it should be noted that the mechanical properties for the PRC with interfacial debonding show evident nonlinear characteristics, and plastic features tend to be strengthened with increasing strain rates. Compared with the loading strain rate

0.0005/s, the strain rates 0.001/s and 0.01/s provide 10.8% and 34.5% respective increases for the stiffness behaviors of the PRC when the true strain increases to 5%.

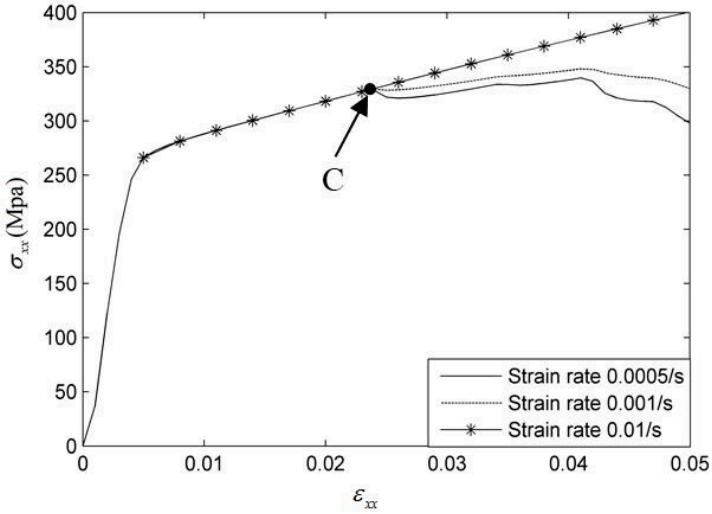

Figure 4. Stress-strain responses of composites with different strain rates.

4. Biaxial Failure Prediction for the PRC with Interfacial Debonding

Interfacial debonding is one of the most common failure forms, which leads to the final failure for composite structures [41,42]. Generally speaking, the macroscopic properties of composites are closely dependent on interfacial properties, while the interphase between particles and matrix is always the weakest bonding. For composites with and without interfacial debonding, there is a huge difference in studying the failure strength. Here, for further investigations of the biaxial failure envelopes of SiC particles and A356 aluminum, only a specific strain rate of 0.0005/s is considered. The corresponding material parameters can be seen in Section 3 and the thermal residual stresses are considered in all cases. The failure strengths of SiC particle and Al matrix are 1000 MPa and 280 MPa [19,36], respectively. The maximum stress criterion [43] is used for investigating the biaxial failure strength.

4.1. Effect of Interfacial Debonding

For investigating the interfacial debonding, perfect interfacial bonding is also used to analyze the effect of the biaxial failure strength for comparison. In Figure 5, the biaxial failure envelopes of the spherical PRC are plotted. For validating the proposed method, the failure strength of experimental data acquired by Lyold [36] in uniaxial tensile loading is also shown in the figure. It can be seen that the theoretical results show good agreement with experimental data only when the interfacial debonding is considered. The relative error is less than 8%. For the PRC with perfect interfacial bonding, the failure envelope is symmetrical about the origin of coordinates (0,0). In the case of compression-compression loading, the interfacial bonding influences on failure strength can be ignored, and the final failure for the PRC is decided by the compressive failure of the reinforced particles. However, the PRC with interfacial debonding show lower failure strength in region I. The interfacial debonding influences on the biaxial failure envelope show different variations in tensile-tensile loading. The failure strength is determined by the interfacial cohesive strength and constituent materials' properties. Meanwhile, the maximum difference of failure strength between perfect interface and interfacial debonding is along the line E'-E.

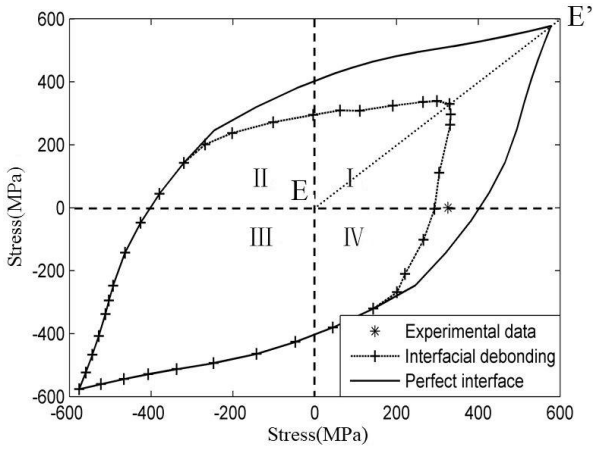

Figure 5. The prediction of biaxial failure strength for the particle-reinforced composites (PRC) with and without interfacial debonding.

4.2. Effect of Interfacial Cohesive Strength

According to the results in Section 3, once the interfacial stress is equal to interfacial cohesive strength, the interface cannot transmit the loadings from the matrix to particles. Therefore, the interfacial strength plays an important role in studying mechanical behaviors. Here, two different interfacial cohesive strengths for the spherical PRC, that is 230 MPa and 330 MPa, are both discussed, as shown in Figure 6. For comparison, the results of the PRC with the interfacial cohesive strength 430 MPa are also shown in the figure. The results by our group [38] indicated that the mechanical properties of composites are decided by matrix properties after completing interfacial failure, and the stress-strain responses of composites with different interfacial cohesive strengths tend to be uniform finally. However, it can be observed from Figure 6 that failure strength is closely dependent on both the interfacial strength and loading conditions. In detail, the failure strength in uniaxial compressive and biaxial compressive loadings is independent of interfacial cohesive strength. The obvious differences can be found in biaxial tensile loadings, where the higher interfacial strength provides the higher failure strength in biaxial and uniaxial tensile loading. This means that the higher stress is needed for the higher interfacial cohesive strength, and more loadings can be loaded on the particles through the matrix materials. For the PRC with interfacial cohesive strengths of 230 MPa and 330 MPa, it is interesting to mention that the effect of the interfacial cohesive strength on the failure envelope is only evident, and to a very limited extent, in tensile-tensile loading.

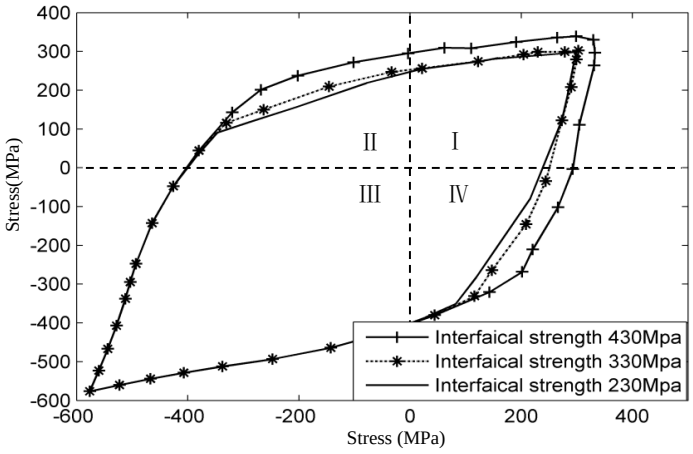

Figure 6. The prediction of biaxial failure envelopes for the PRC with different interfacial cohesive strength.

4.3. Effect of Particle Shape

Particle shape plays an important role in mechanical behaviors for the PRC. However, few research studies refer to the particle shape influences on the biaxial failure envelopes of the PRC with interfacial debonding. Here, three different particle shapes, as shown in Section 3.3, are considered in the cases listed in this study, and the prediction results can be observed in Figure 7. It can be seen from the figure that the biaxial failure envelopes of the PRC are closely related to the particle shape, while the particle shapes' influence on failure strength is only evident to a limited extent in the failure surface. The particle shapes' influences on uniaxial failure strength in tensile and compressive loading show different variations along the semi-major direction. The higher failure strength can be acquired with increasing semi-major axis ratios in uniaxial compressive loading. Compared with the spherical particle-reinforced composites, the failure strength of ellipsoid particle-reinforced composites with semi-major axis ratio 1.5 provide a nearly 8% increase in uniaxial compressive loading. However, it is difficult for researchers to discern the failure strength difference among the three different particle shapes in uniaxial tensile loading along with the semi-major axis, and only a little difference can be found in uniaxial tensile and compressive loadings.

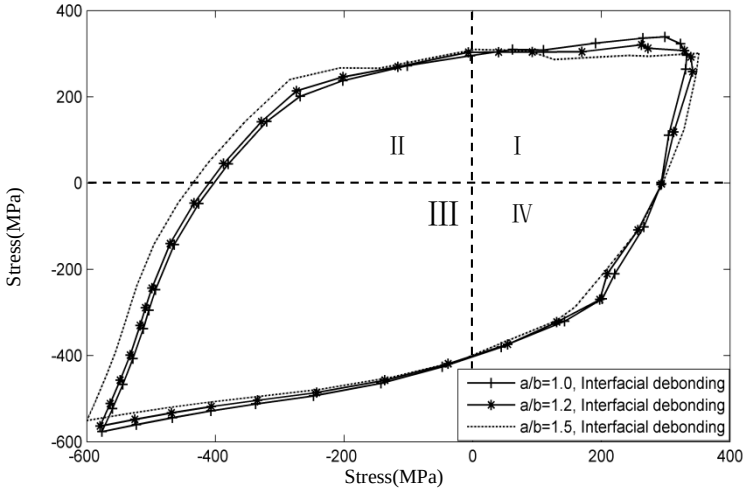

Figure 7. The prediction of biaxial failure envelops for the PRC with different particle shapes.

5. Conclusions

In the present study, the particles were distributed regularly in the matrix materials. An effective microscopic mechanical model was improved to investigate the nonlinear stress-strain properties of particle-reinforced composites with consideration of the evolution of interfacial debonding. The theoretical result shows good agreement with the experimental data. On this basis, the interfacial debonding influences on biaxial failure properties were also investigated, and the results can be concluded as follows:

(1) The micromechanical model can be used to predict mechanical properties of the PRC with interfacial debonding effectively.
(2) The particle volume fraction effects on stiffness behaviors for the PRC with and without interfacial debonding show different variations. The stiffness behaviors become softer with the increasing volume fraction in some regions when the interfacial debonding is considered.
(3) The SiC particle-reinforced A356 aluminum composites with interfacial debonding show obvious rate-dependency of the deformation, and higher strain rates increase the stiffness properties.
(4) For the PRC in the compression-compression biaxial loading, interfacial bonding's influences on failure strength can be ignored. However, the obvious difference can be seen in the tensile-tensile loading.

(5) The higher interfacial strength of particle-reinforced composites tends to increase the biaxial failure strength, while the obvious differences can only be found in regions I, II, and IV.

Acknowledgments: This work was supported by the National Natural Science Foundation of China (No. 51675397, 51305320, 51505364), Natural Science Basic Research Plan in Shaanxi Province of China (No. 2015JQ5146), and Fundamental Research Funds for the Central Universities (JB150402).

Author Contributions: Junjie Ye, Chenchen Chu and Zhi Zhai established the microscopic model, and Junjie Ye wrote the paper. Yongkun Wang and Yuanying Qiu investigated the nonlinear behaviors of composites with consideration of interphase influences. Baoquan Shi studied the effects of interfacial cohesive strength and modified the grammar mistakes.

Conflicts of Interest: The authors declare no conflict of interest.

References

1. Wang, Y.; Ye, J.; Tian, W. Shape memory polymer composites of poly (styrene-*b*-butadiene-*b*-styrene) copolymer/liner low density polyethylene/Fe_3O_4 nanoparticles for remote activation. *Appl. Sci.* **2016**, *333*, 333–341. [CrossRef]
2. Teng, H. Prediction of the effective Young's modulus of a particulate composite containing fractured particles. *Finite Elem. Anal. Des.* **2013**, *65*, 32–38. [CrossRef]
3. Cao, Y.; Feng, Y.; Wang, W. Estimation of lamina stiffness and strength of quadriaxial non-crimp fabric composites based on semi-laminar considerations. *Appl. Sci.* **2016**, *6*, 267–283. [CrossRef]
4. Ludovic, R.; Moukrane, D.; Sophie, G.; Jérôme, D.; David, T.; Elisabeth, A.G. Structure evolutions in a Ti–6Al–4V matrix composite reinforced with TiB, characterised using high energy X-ray diffraction. *J. Alloys Compd.* **2015**, *624*, 179–188.
5. Chen, Q.; Chen, X.; Zhai, Z.; Yang, Z. A new and general formulation of three-dimensional finite-volume micromechanics for particulate reinforced composites with viscoplastic phases. *Compos. B Eng.* **2016**, *85*, 216–232. [CrossRef]
6. Kargar, M.; Behravesh, A.H.; Taheri, H.M. Experimental investigation on mechanical properties of extruded foamed pvc-wood composites reinforced with continuous glass fibers. *Polym. Compos.* **2016**, *37*, 1674–1680. [CrossRef]
7. Taupin, V.; Berbenni, S.; Fressengeas, C.; Bouaziz, O. On particle size effects: An internal length mean field approach using field dislocation mechanics. *Acta Mater.* **2010**, *58*, 5532–5544. [CrossRef]
8. Thomas, P.C.; Jose, T.E.; Thomas, S.P. High-performance nanocomposites based on arcylonitrile-butadiene rubber with fillers of different particle size: mechanical and morphological studies. *Polym. Compos.* **2010**, *31*, 1515–1524. [CrossRef]
9. Diler, E.A.; Ipek, R. Main and interaction effects of matrix particle size, reinforcement particle size and volume fraction on wear characteristics of Al–SiCp composites using central composite design. *Compos. B Eng.* **2013**, *50*, 371–380. [CrossRef]
10. Kumar, K.R.; Mohanasundaram, K.M.; Arumaikkannu, G. Effect of particle size on mechanical properties and tribological behaviour of aluminium/fly ash composites. *Sci. Eng. Compos. Mater.* **2012**, *19*, 247–253. [CrossRef]
11. Saito, A.; Takahashi, H. The influence of filler geometrical shape on the friction and wear of particle filled polymers. *Sci. Eng. Compos. Mater.* **1997**, *6*, 95–109. [CrossRef]
12. Rasool, A.; Böhm, H.J. Effects of particle shape on the macroscopic and microscopic linear behaviors of particle reinforced composites. *Int. J. Eng. Sci.* **2012**, *58*, 21–34. [CrossRef]
13. Bourkas, G.; Prassianakis, I.; Kytopoulos, V.; Sideridis, E.; Younis, C. Estimation of elastic moduli of particulate composites by new models and comparison with moduli measured by tension, dynamic, and ultrasonic tests. *Adv. Mater. Sci. Eng.* **2010**, *2010*, 1–13. [CrossRef]
14. Galli, M.; Cugnoni, J.; Botsis, J. Numerical and statistical estimates of the representative volume element of elastoplastic random composites. *Eur. J. Mech. A. Solids* **2012**, *33*, 31–38. [CrossRef]
15. Han, G.; Guan, Z.; Ji, Z.; Du, S. Initial damage induced by thermal residual stress and microscopic failure analysis of carbon-fiber reinforced composite under shear loading. *Compos. Interfaces* **2015**, *22*, 315–329. [CrossRef]

16. Xu, K.; Qian, X. An FEM Analysis with Consideration of random void defects for predicting the mechanical properties of 3D braided composites. *Adv. Mater. Sci. Eng.* **2014**, *2014*, 1921–1926. [CrossRef]
17. Gao, H.; Huang, Y. Taylor-based nonlocal theory of plasticity. *Int. J. Solids Struct.* **2001**, *38*, 2615–2637. [CrossRef]
18. Huang, Y.; Qu, S.; Hwang, K.C.; Li, M.; Gao, H. A conventional theory of mechanism-based strain gradient plasticit. *Int. J. Plast.* **2004**, *20*, 753–782. [CrossRef]
19. Abedini, A.; Chen, Z.T. A micromechanical model of particle-reinforced metal matrix composites considering particle size and damage. *Comput. Mater. Sci.* **2014**, *85*, 200–205. [CrossRef]
20. McWilliams, B.A.; Ramesh, K.T.; Yen, C.F. Probabilistic response of heterogeneous particle reinforced metal matrix composites with particle size dependent strengthening. *Comput. Mater. Sci.* **2013**, *79*, 15–24. [CrossRef]
21. Zhang, X.X.; Xiao, B.L.; Andrä, H.; Ma, Z.Y. Homogenization of the average thermo-elastoplastic properties of particle reinforced metal matrix composites: The minimum representative volume element size. *Compos. Struct.* **2014**, *113*, 459–468. [CrossRef]
22. Moumen, A.E.; Imad, A.; Kanit, T.; Hilali, E.; Minor, H.E. A multiscale approach and microstructure design of the elastic composite behavior reinforced with natural particles. *Compos. B Eng.* **2014**, *66*, 247–254. [CrossRef]
23. Mandal, D.; Viswanathan, S. Effect of re-melting on particle distribution and interface formation in SiC reinforced 2124Al matrix composite. *Mater. Charact.* **2013**, *86*, 21–27. [CrossRef]
24. Sideridis, E. The influence of particle distribution and interphase on the thermal expansion coefficient of particulate composites by the use of a new model. *Compos. Interfaces* **2016**, *23*, 231–254. [CrossRef]
25. Lee, H.K.; Pyo, S.H. Micromechanics-based elastic damage modeling of particulate composites with weakened interfaces. *Int. J. Solids Struct.* **2007**, *44*, 8390–8406. [CrossRef]
26. Zhou, R.J.; Thomas, B. Polypropylene/SiO_2 nanocomposites filled with different nanosilicas: Thermal and mechanical properties, morphology and interphase characterization. *J. Mater. Sci.* **2011**, *46*, 1228–1238. [CrossRef]
27. Hutar, P.; Majer, Z.; Nahlik, L.; Shestakova, L.; Knesl, Z. Influence of particle size on the fracture toughness of a PP-based particulate composite. *Mech. Compos. Mater.* **2009**, *45*, 281–286. [CrossRef]
28. Shao, J.C.; Xiao, B.L.; Wang, Q.Z.; Ma, Z.Y.; Yang, K. An enhanced FEM model for particle size dependent flow strengthening and interface damage in particle reinforced metal matrix composites. *Compos. Sci. Technol.* **2011**, *71*, 39–45. [CrossRef]
29. Yuan, Z.; Li, F.; Xue, F.; He, M.; Hussain, M.Z. Analysis of the stress states and interface damage in a particle reinforced composite based on a micromodel using cohesive elements. *Mater. Sci. Eng. A* **2014**, *589*, 288–302. [CrossRef]
30. García, I.G.; Mantič, V.; Graciani, E. A model for the prediction of debond onset in spherical-particle-reinforced composites under tension. Application of a coupled stress and energy criterion. *Compos. Sci. Technol.* **2015**, *106*, 60–67. [CrossRef]
31. Aghdam, M.M.; Shahbaz, M. Effects of interphase damage and residual stresses on mechanical behavior of particle reinforced metal-matrix composites. *Appl. Compos. Mater.* **2014**, *21*, 429–440. [CrossRef]
32. Majer, Z.; Hutar, P.; Nahlik, L. Determination of the effect of interphase on the fracture toughness and stiffness of a particulate polymer composite. *Mech. Compos. Mater.* **2013**, *49*, 475–482. [CrossRef]
33. Aboudi, J.; Arnold, S.M.; Bednarcyk, B.A. *Micromechanics of Composite Materials—A Generalized Multiscale Analysis Approach*; Elsevier: New York, NJ, USA, 2013.
34. Aboudi, J. *Mechanics of Composite Materials—A Unified Micromechanical Approach*; Elsevier: London, UK, 1991.
35. Bednarcyk, B.A.; Arnold, S.M. Micromechanics-based deformation and failure prediction for longitudinally reinforced titanium composites. *Compos. Sci. Technol.* **2001**, *61*, 705–729. [CrossRef]
36. Lloyd, D.J. Particle reinforced aluminum and magnesium matrix composites. *Int. Mater. Rev.* **1994**, *39*, 1–23. [CrossRef]
37. Qu, S.; Siegmund, T.; Huang, Y.; Wu, P.D.; Zhang, F.; Hwang, K.C. A study of particle size effect and interface fracture in aluminum alloy composite via an extended conventional theory of mechanism-based strain-gradient plasticity. *Compos. Sci. Technol.* **2005**, *65*, 1244–1253. [CrossRef]
38. Ye, J.; Chen, X.; Zhai, Z.; Li, B.; Zi, Y.; He, Z. Effects of thermal stress and imperfect interfacial bonding on the mechanical behavior of composites subjected to off-axis loading. *Mater. Sci. Eng. A* **2010**, *527*, 7530–7537. [CrossRef]

39. Chen, X.F.; Ye, J.J.; Zhai, Z.; Duan, Y.G.; He, Z.J. Micromechanical analysis of off-axis loading of fiber reinforced composites with imperfect interface bonding. *Int. J. Mech. Sci.* **2012**, *54*, 113–120. [CrossRef]
40. Yang, B.J.; Kim, B.R.; Lee, H.K. Predictions of viscoelastic strain rate dependent behavior of fiber-reinforced polymeric composites. *Compos. Struct.* **2012**, *94*, 1420–1429. [CrossRef]
41. Shams, A.; Porfiri, M. Analysis of particle–matrix interfacial debonding using the proper generalized decomposition. *Compos. Struct.* **2014**, *111*, 602–618. [CrossRef]
42. Ye, J.J.; Qiu, Y.Y.; Chen, X.F.; Ma, J.; Zhai, Z. Working temperature variation effect on the failure envelope of continuous fiber-reinforced composites. *Compos. Interfaces* **2015**, *22*, 531–542. [CrossRef]
43. Tang, Z.; Zhang, B. Prediction of biaxial failure envelopes for composite laminates based on Generalized Method of Cells. *Compos. B Eng.* **2012**, *43*, 914–925. [CrossRef]